ACS APPLIED MATERIALS & INTERFACES

www.acsami.org

Research Article

Mechanistic Insight and Local Structure Evolution of $NiPS_3$ upon Electrochemical Lithiation

Christopher Choi,* David Ashby, You Rao, Elaf Anber, James L. Hart, Danielle Butts, Catrina Wilson, Emily Levin, Mitra Taheri, Maryam Ghazisaeidi, Bruce Dunn, and Vicky Doan-Nguyen*

Cite This: *ACS Appl. Mater. Interfaces* 2022, 14, 3980−3990

Read Online

ACCESS | Metrics & More | Article Recommendations | Supporting Information

ABSTRACT: Transition metal phosphorus trisulfide materials have received considerable research interest since the 1980−1990s as they exhibit promising energy conversion and storage properties. However, the mechanistic insights into Li-ion storage in these materials are poorly understood to date. Here, we explore the lithiation of $NiPS_3$ material by employing *in situ* pair-distribution function analysis, Monte Carlo molecular dynamics calculations, and a series of *ex situ* characterizations. Our findings elucidate complex ion insertion and storage dynamics around a layered polyanionic compound, which undergoes intercalation and conversion reactions in a sequential manner. This study of $NiPS_3$ material exemplifies the Li-ion storage mechanism in transition metal phosphorus sulfide materials and provides insights into the challenges associated with achieving reliable, high-energy phosphorus trisulfide systems.

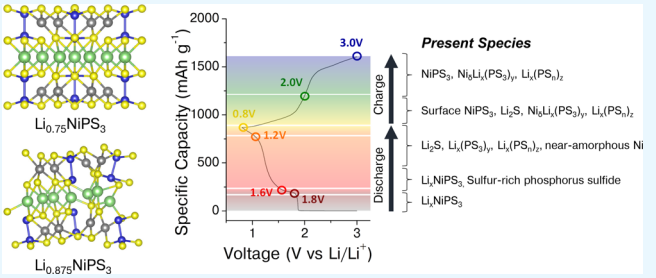

KEYWORDS: *2D materials, metal phosphorus trichalcogenides, Li-ion insertion mechanism, intercalation reactions, conversion reactions*

INTRODUCTION

In recent years, transition metal chalcogenides (MX_z, where M = V,[1,2] Mn, Fe,[3,4] Co,[5,6] Ni, Cd, Mg, Zn, Mo[7,8] and X = S, Se), carbides,[9] and nitrides[10,11] ($M'_{n+1}A_nT_x$, where A = C or N and T = H, OH) have been extensively investigated as active materials for various electrochemical energy storage applications such as lithium-ion (Li-ion), sodium-ion (Na-ion), and lithium−sulfur (Li−S_x) based storage and metal−air batteries. One approach to design a new layered electrode material system for improved electrochemical performance is the modification of the electronic structure of 3d-metal centers by tuning its covalency and electronegativity.[12] Generally, by introducing polyanions in the material structure (i.e., oxysulfides), as opposed to a single anion (i.e., oxides and sulfides), an inductive effect is observed as a result of the change in distribution of electrons in a M−X bond, leading to an increase of the reduction−oxidation (redox) potentials.[13,14]

Transition metal phosphorus trichalcogenides (MPX_3) are a potential polyanionic active material with the material having the $CdCl_2$-type layered structure (compact stacking of sulfur layers of ABC type), in which one-third of the transition metals are substituted by P−P pairs within the layers. Each $[P_2X_6]^{4-}$ unit occupies the center of six divalent transition metal ions M^{2+} forming a hexagonal lattice, leading to the general formula of $M_2P_2X_6$. In contrast to the transition metal dichalcogenides, MPX_3 compounds generally have a larger van der Waals gap (>6 Å) such that Li-ion intercalation would have a minimal effect on the lattice parameters. By analogy with the layered TiS_2 system, it was hypothesized that the intercalated Li-ions would sit in octahedral sites in the van der Waals gaps, leading to a theoretical maximum of 1.5 Li-ions in between each MPX_3 layer.[15] Among various MPS_3 host systems with attainable transition metal centers (M = V, Mn, Fe, Co, Ni, Zn, Cd), $NiPS_3$, $FePS_3$, and $CoPS_3$ have shown to chemically intercalate Li-ions without kinetic limitations.[16] This observation has been attributed to the ionic character, therefore the band energy level, of the M−S bond.[17] For transition metals with higher bond ionicity, such as Ni, Fe, and Co, cationic electron transfers occur more readily from the lower Hubbard bands.[18] Thus, the site potential in the host lattice is minimal in $NiPS_3$ due to the highest bond ionicity, leading to rapid Li-ion diffusion in the material and best electrochemical intercalation behavior.

In the 1970−1980s, significant effort was invested to explore Li-ion storage properties and chemical changes associated with it in $NiPS_3$ compounds.[18−21] These early studies established reversible chemical and electrochemical insertion of a few Li-ions, but subsequent studies also revealed that the electrochemical redox reaction is not limited to the available redox

Received: October 15, 2021
Accepted: December 28, 2021
Published: January 11, 2022

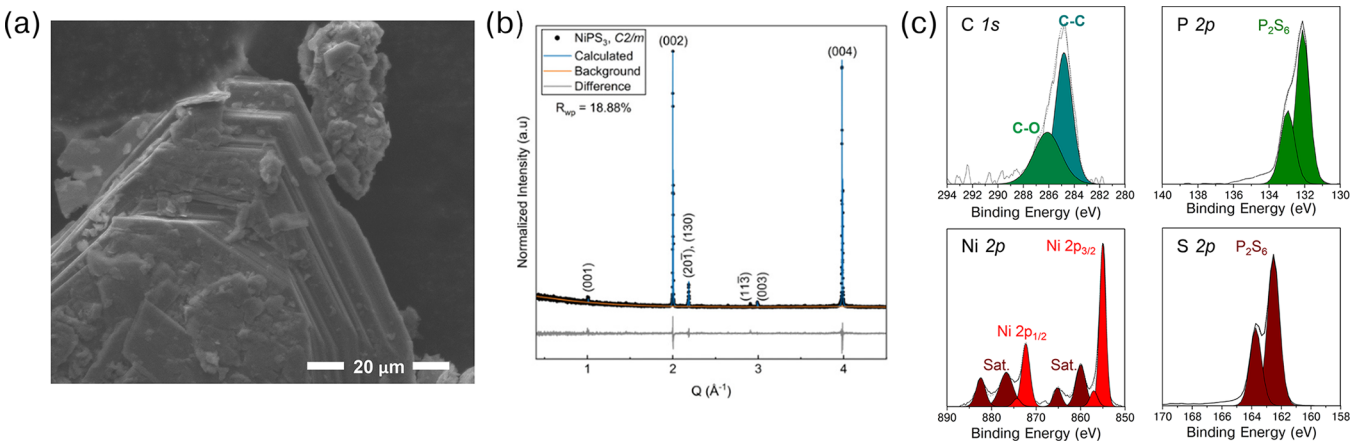

Figure 1. Material characterization of as-prepared $NiPS_3$. (a) Morphology and microstructural characteristics observed by using SEM. (b) XRD confirms phase purity with preferred orientation in the (002) direction. (c) Surface chemical composition and bonding configuration probed by XPS. Ni 2p, S 2p, and P 2p binding energies are fitted to chemical states of spin−orbit components.

states on the transition metal and can continue with reasonable reversibility up to more than eight Li-ions with the proposed overall reaction: $NiPS_3 + 9Li^+ + 9e^- \leftrightarrow 3Li_2S + Li_3P + Ni$.[22,23] However, the charge storage mechanism and redox reaction characteristics around redox-active centers are still unclear, highlighting the need for an in-depth mechanistic study focused on electrochemical Li uptake in $NiPS_3$ compounds. A brief overview of Li-ion storage characteristics of various nickel sulfides and phosphides is presented in Table S1.[24−26]

Here, we report mechanistic and structural evolution of $NiPS_3$ upon electrochemical Li-ion insertion by employing a library of *operando* and *ex situ* spectroscopic techniques. The electrochemical redox potential range investigated in our study was less than the theoretical capacity for full reduction of the cationic center and surrounding anions (nine Li-ions) but much greater than that for solid−solution intercalation reaction. Probing dual intercalation and conversion reaction pathways in the polyanionic active material involving redox reactions of three elements is far more complex to systemically study than similar electrochemical activities in the binary material. Although this could be a significant challenge, insight into and clarification of the fundamental insertion reaction mechanisms in the polyanionic materials are important steps toward enabling rational material design for advanced energy storage applications. Therefore, we use *operando* pair distribution function (PDF) and electrochemical methods to elucidate the initial lithium intercalation reaction and a combination of various *ex situ* characterization techniques to identify the subsequent conversion reaction pathways.

RESULTS AND DISCUSSION

Material Synthesis and Structure. Solid-state chemical synthesis was performed using elemental precursors in stoichiometric ratios to produce $NiPS_3$ starting material. Sealed quartz ampules of precursor components were reacted in Ar atmosphere to prevent oxidized products similar to previously reported methodologies.[16] Figure 1 and Figure S1 show the physical and structural characteristics of the as-synthesized $NiPS_3$ material. The phase was first examined by powder X-ray diffraction (XRD). Pawley refinements based on the standard $C2/m$ space group were performed to confirm the purity and determine the lattice parameters.

Pawley refinement was performed due to the large amount of preferred orientation in the (002) direction as evidenced by the high-intensity (002) and (004) reflections and low-intensity (001) reflection. Refinement indicated plate-like orientation by the resulting March−Dollase preferred orientation ratio of 0.40(6), which SEM confirmed as represented in Figure 1a. Because of this, the parameter-weighted goodness-of-fit value, R_{wp} = 18.88%, is relatively large (Figure 1b). The refined lattice parameters are as follows: a = 5.88(3) Å, b = 10.164(2) Å, c = 6.66(3) Å, and b = 107.91(8)°. These agree well with previously reported lattice parameters.[24] The small uncertainty values in the lattice parameters illustrate a good fit to the $C2/m$ space group. From the lack of impurity peaks, the small uncertainty values in the lattice parameters, and the agreement between the refined lattice parameters and previously reported crystal structures phase purity of the as-synthesized $NiPS_3$ can be concluded.

X-ray photoelectron spectroscopy (XPS) was performed to study the surface chemical composition and bonding configuration. The oxidation states of Ni, P, S, and C were probed. The XPS spectrum in the Ni 2p region (Figure 1c) shows two sets of three peaks at higher (872.1, 876.6, and 882.3 eV) and lower binding energies (854.6, 859.8, and 865.1 eV), corresponding to the $2p_{3/2}$ (854.8 eV) and $2p_{1/2}$ (872.0 eV) core levels of Ni^{2+}.[27,28] Each of the spin−orbit involves two satellite peaks, which is indicative of the ligand−metal hybridization between the polyanion cluster and transition metal.[28,29] The characteristic peaks for both the P 2p and S 2p scans show a spin−orbit split doublet into $2p_{3/2}$ and $2p_{1/2}$ orbitals (P 2p $2p_{3/2}$ = 132.1, $2p_{1/2}$ = 132.9 eV and S 2p $2p_{3/2}$ = 162.5, $2p_{1/2}$ = 163.7 eV, respectively), which is consistent with previous XPS measurements on $NiPS_3$.[30]

Electrochemical Performance Testing. Galvanostatic profiles and cyclic voltammetry (CV) of the $NiPS_3$ (mass loading ≈ 1−2 mg cm^{-2}) are shown in Figures 2a and 2b, respectively. The lower cycling potential limit was set to 0.8 V vs Li/Li^+ to avoid most side reactions involving the reduction decomposition of the electrolyte, which could complicate the chemical analysis of our system.[31] Also, the formation of the fully reduced transition metal phase (biased potential toward 0 V) is known to be detrimental for the electrochemical reversibility and Coulombic efficiency.[32] For the galvanostatic cycling between 3.0 V (open-circuit potential, OCV) and 0.8

https://doi.org/10.1021/acsami.1c19963
ACS Appl. Mater. Interfaces 2022, 14, 3980−3990

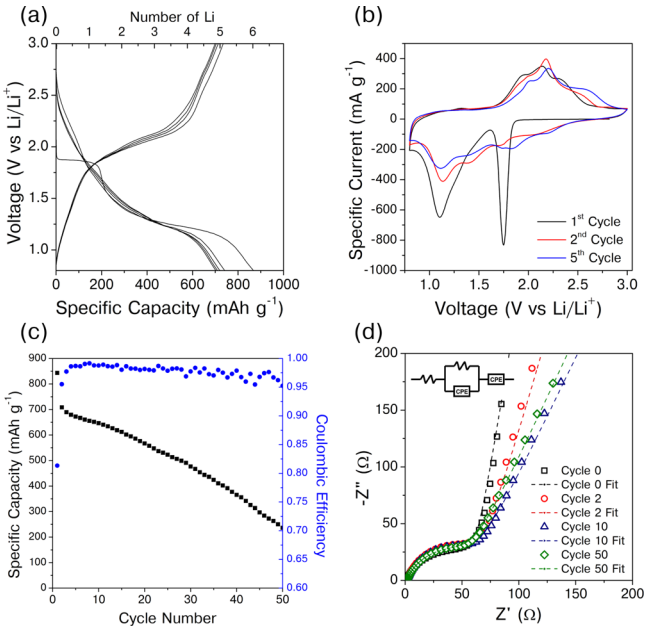

Figure 2. Electrochemical characterization of $NiPS_3$ in 1 M $LiPF_6$ EC:DMC 1:1 mixture using a half-cell configuration. (a) Initial five galvanostatic charge−discharge curves at a constant current density of 100 mA g^{-1}. (b) Cyclic voltammogram of $NiPS_3$ cycled between 0.8 and 3.0 V at a sweep rate of 0.1 mV s^{-1}. Cycles 1, 2, and 5 are shown. (c) Capacity and Coulombic efficiency per cycle obtained from the galvanostatic cycling. (d) Impedance spectra of $NiPS_3$ electrodes at various cycles. Each data set was fit by using an equivalent circuit shown in the inset.

V, the first discharge curve exhibits a distinct, flat plateau at 1.9 V, characteristic of a two-phase reaction. After the initial plateau, a voltage drop is observed followed by another nearly plateau-like curve at 1.4 V until about four Li-ions are inserted per formula unit. Then the voltage sharply drops to 0.8 V with further insertion of Li-ions. The specific capacity observed from the first cycle down to 0.8 V is 871 mAh g^{-1}, which corresponds to insertion of six Li-ions. As for the deinsertion of Li-ions, a plateau-like curve at around 2.0 V was observed, and the voltage profile is reversible for a limited number of cycles (80% initial capacity at cycle 5). After the first cycle, the discharge voltage plateau at 1.9 V disappears. It is typical for the first discharge plateau of conversion materials to differ from the first cycle in subsequent discharges.[32] This irreversible behavior, in general, has been attributed to the formation of many nanoscale domains and of new interfaces during the first discharge.[33] The disappearance of the 1.9 V plateau in the $NiPS_3$ discharge curve appears to depend on the current density at which the cell is cycled, and this has been addressed in the previous literature.[34]

A cyclic voltammogram with a sweep rate of 0.1 mV s^{-1} reveals two cathodic peaks at 1.75 and 1.1 V and broad anodic peaks around 2 V from the first cycle. The cathodic peak at 1.75 V disappears for subsequent cycles, and all remaining cathodic peaks become less pronounced. Based on the current response from CV measurement, about six Li-ions are inserted in the potential range between 0.8 and 3.0 V, which is in good agreement with galvanostatic experiments. Charging and discharging of $NiPS_3$ in this potential range confirms to be a multielectron process involving the redox of the Ni^{2+} cation and $(PS_3)^{2-}$ anion based on the large voltammetric current responses.

Similar to typical lithium−sulfur and other conversion-based electrode cells, unsatisfactory capacity retention and poor long-term cyclability are observed (Figure 2c). Over the period of 50 cycles, a steady decrease in discharge capacity occurs. The gravimetric capacity upon the fiftieth discharge is 236.25 mAh g^{-1}, which corresponds to about 30% capacity retention. Figure S2 compares the Li-ion charge storage of $NiPS_3$ at *C*-rates ranging from *C*/5 to 2*C*. As expected, $NiPS_3$ materials demonstrate fair rate capability over the 0.8−3.0 V (vs Li/Li^+) range, reaching gravimetric capacities of 528.9 and 287.8 mAh g^{-1} at 1*C* and 2*C*, respectively. The initial electrochemical results, such as poor long-term performance and sluggish insertion kinetics, show archetypal characteristics of the conversion-based Li-ion storage mechanism that accompanies a large volume expansion of electrode materials during the discharge/charge process. Analysis of electrochemical impedance spectroscopy measurements suggests consistent series resistance at 3 V for 50 cycles, which is indicative of stable SEI in the operating voltage window. This observation also suggests that the poor long-term cyclability is not due to the degradation of the electrolytes or growth of the solid−electrolyte interphase layers but is likely due to the decomposition of the $NiPS_3$ active material.

Local Structural Changes during the Intercalation Process. For the layered materials with a viable transition metal redox center, electrochemically inserted Li-ions are preferably stored in the van der Waals gap.[35] Traditionally, monitoring the lithium intercalation in the layered structure has been done via X-ray diffraction by looking at the peak shifts/evolution accompanying structural changes or expansion in the interlayer spacing.[36] However, in the case of MPX_3 materials, the absence of structural changes upon lithium insertion in the intercalation region makes the characterization trickier compared with other layered hosts. To this end, *operando* total scattering with PDF analysis is used to reveal the local environments and short-range ordering of $NiPS_3$ upon Li-ion insertion. PDF analysis has previously been demonstrated to be an invaluable method for discerning local structure evolution of as-prepared active materials and cycled products.[2,5,8,37,38] *Operando* PDFs have revealed chemical moieties that have illuminated Li-ion insertion mechanisms that contained dual modes of intercalation and conversion.[37]

To probe the local structural evolution, *operando* PDF of a cycling $NiPS_3$ cell was collected at a rate of 40 mA g^{-1} over the first nine cycles. The electrochemical voltage range was selected such that $NiPS_3$ was subjected to reversible insertion/deinsertion of less than 1 mol of Li^+ to avoid any conversion reactions beyond the intercalation regime. Despite an initial claim over the theoretical intercalation limit of $x = 1.5$ (Li_xNiPS_3), previous *ex situ* XRD and NMR studies suggested the appearance of a second crystalline phase and change in its magnetic property around or before $x = 1$, which is indicative of the beginning of new phase evolutions.[39,40] It should be pointed out that the electrochemical cycling results obtained during the *operando* measurement exhibit a highly polarized gravimetric voltage signature. This electrochemical response has been attributed to the low electrical conductivity of $NiPS_3$ compound ($\sim 10^{-9}$ S cm^{-1})[41,42] and high mass loading electrode (16.9 mg cm^{-2}) required to obtain an adequate signal for the total X-ray scattering experiments.[8,43] The limited lithiation of $NiPS_3$ over the similar voltage window has also been observed in an all-solid-state system and was

https://doi.org/10.1021/acsami.1c19963
ACS Appl. Mater. Interfaces 2022, 14, 3980−3990

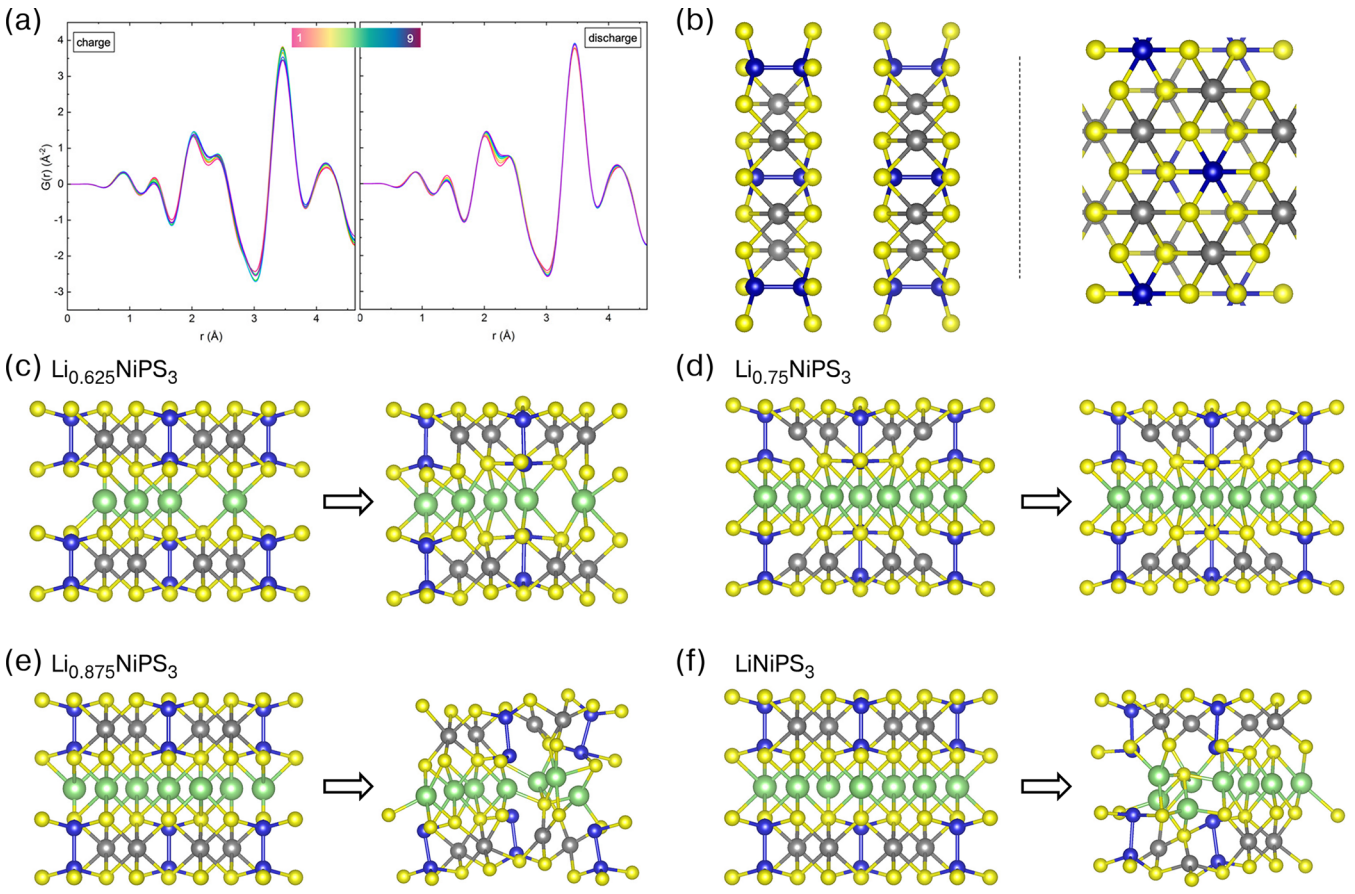

Figure 3. (a) Overlay of extracted PDFs across nine cycles from charge at 3.0 V and discharge at 1.0 V vs Li/Li^+ demonstrates minimal changes in local structure, up to 4.5 Å, for $NiPS_3$. (b) Structure of the multilayer $NiPS_3$: side view (left) and top view (right). (c–f) Stability of the layered structure. Phase transformation occurs as the amount of Li increases. (c) $Li_{0.625}NiPS_3$, (d) $Li_{0.75}NiPS_3$, (e) $Li_{0.875}NiPS_3$, and (f) $LiNiPS_3$. Colors: green = Li, yellow = S, blue = P, and gray = Ni.

attributed to the low active material electrical conductivity and high interfacial resistance.[44]

An interesting observation here is that for the intercalation regime of $NiPS_3$ the PDF does not change over the period of six lithiation/delithiation cycles. Previously, ^{31}P NMR of $NiPS_3$ demonstrated the unchanging peak center and shape for intercalation of $x < 0.5$ in Li_xNiPS_3, indicating a lack of local structure shift and minimal oxidation state change.[39,45] Further analysis of this PDF series signals about 0.8 mol of Li has been intercalated with minimal structural changes up to 4.5 Å, indicating the avoidance of conversion reactions or phase transition, occupying possible Li-ion intercalation sites (2d, 4h, 8j, 4h, 2c, 4i) (Figure 3a and Figure S3). The local structure can be retained as previously proposed by Chianelli and Dines in which transition-metal trichalcogenides are exfoliated and only lose long-range ordering upon Li-ion intercalation.[46] From optical spectroscopy (Figure S4), it was observed that smaller crystals formed from striated larger crystals. Given the larger layer spacing of the $NiPS_3$ structure, the Li-ion is the appropriate size to occupy the octahedral interstices, and the intercalation of Li-ion into these sites would not cause any stress to the crystal structure.[20]

The intercalation process of Li-ions into $NiPS_3$ structure was further investigated via the plane-wave-based density functional theory (DFT) package VASP. As shown in Figure 3b, our simulation cell has 8 Ni atoms, 8 P atoms, and 24 S atoms forming two layers of $NiPS_3$ with an interplanar distance of 3.389 Å. A vacuum of 20 Å is included to avoid the interaction between periodic images. After relaxation, Li-atoms are incrementally added to the Wyckoff sites, from 5 Li to 24 Li, corresponding to stoichiometries from $Li_{0.625}NiPS_3$ to Li_3NiPS_3. Despite the certain site preference for Li (Figure S5), the Li-atoms are not assigned to those favorable sites due to possible interactions between them, especially at higher concentrations. Instead, a Monte Carlo method is used to determine the favorable configuration for each composition.[47,48] First, the simulation cells are constructed for a given concentration with Li-atoms randomly occupying the Wyckoff sites. Next, the atomic positions of a Li-atom and a vacant Wyckoff site are swapped, both of which are randomly chosen. Then the energy change associated with this Monte Carlo move ΔE is calculated, and this move is accepted with a probability $p = \min\{1, \exp(-\Delta E/k_BT)\}$. Finally, this process is repeated until convergence has been reached. During the Monte Carlo steps, the atomic positions are not allowed to relax. After finding the favorable Li sites, these atoms are relaxed in search for the ground state. As can be seen in Figure 3c–f, both $Li_{0.625}NiPS_3$ and $Li_{0.75}NiPS_3$ maintain the layered structures without any phase transformation. Starting from $Li_{0.875}NiPS_3$, significant distortion is observed. As the concentration of Li reaches $x = 1$ ($LiNiPS_3$), the layered structure breaks down and excessive Li-atoms are ejected out of the central plane, suggesting a phase transition should take place at higher concentrations of Li. This is consistent with the

https://doi.org/10.1021/acsami.1c19963
ACS Appl. Mater. Interfaces 2022, 14, 3980–3990

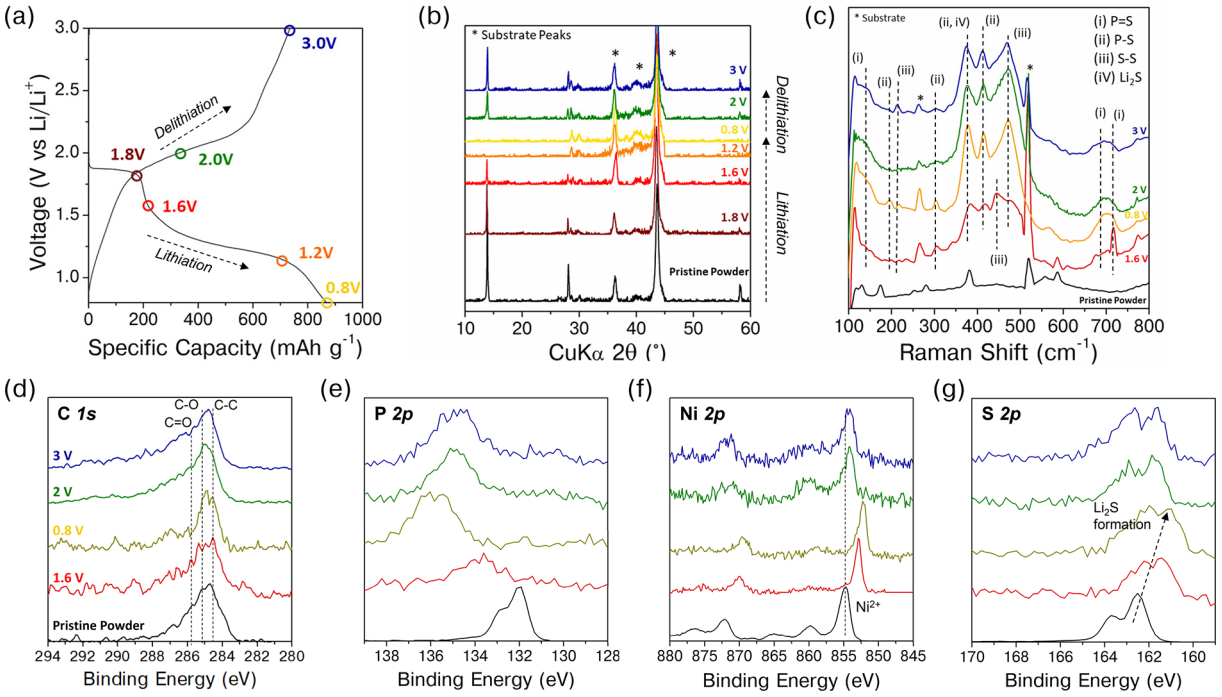

Figure 4. (a) Charge−discharge curve for the first cycle. Cells for the *ex situ* measurements were cycled to the potentials indicated. (b) *Ex situ* XRD patterns showing the evolution of crystalline phases upon lithium intercalation/deintercalation. (c) *Ex situ* Raman spectroscopy of $NiPS_3$ electrodes at various states of charge/discharge. *Ex situ* XPS spectra of (d) C 1s, (e) P 2p, (f) Ni 2p, and (g) S 2p. The general trend is observed that upon lithium insertion the Ni 2p and S 2p peaks shift toward lower binding energies while P 2p lines shift toward higher binding energies.

experimental results that phase transition happens for about 0.8 mol of lithium intercalation.

Two possible explanations for the limited intercalation behavior are the low oxidation state of the Ni d-band center and the thermodynamic instability of sulfide-based materials. The available valence state of Ni upon Li insertion is +1 or 0, given that the host $NiPS_3$ starts with Ni(II). Although Ni(I) is attainable, thermodynamically stable Ni(I) compounds have been exclusively seen in a highly coordinated bonding environment with organic moieties.[49] In addition, a recent computational study has shown that, generally, the thermodynamic driving forces for conversion reactions are higher than those for intercalation reactions in sulfides.[50] Both of these factors are unfavorable in accommodating a large amounts of cations and facilitating potential structural lattice reconstruction to reduce intercalation-induced stress.

Chemical and Phase Evolution during the Conversion Reactions ($x > 0.8$). With continuous lithium insertion beyond $x = 0.8$, substantial structural and chemical evolutions were observed from *ex situ* XRD, XPS, Raman, electron energy-loss spectroscopy (EELS), and high-resolution transmission electron microscopy (HRTEM). For *ex situ* characterization, samples were prepared just prior to measurements and without any exposure to air to minimize changes of the material between cycling and measurements. The discharge−charge curves for the first cycle are shown in Figure 4a and are marked at each point a cell was prepared for *ex situ* measurements.

The *ex situ* XRD patterns of the $NiPS_3$ electrode during the first lithiation and delithiation of an ∼1−2 mg cm^{-2} electrode are shown in Figure 4b. In general, the peaks corresponding to the $NiPS_3$ phase decrease upon lithiation, while two new peaks corresponding to the Li_2S phase appear around 1.6 V (2θ = 28°, 31°) and continue to grow until 0.8 V is reached. This observation indicates that the $NiPS_3$ phase is electrochemically converted into decomposition products including Li_2S and other noncrystalline phases when the cell is discharged below 1.6 V with the insertion of 1.5 Li-ions. The formation of the Li_2S phase as well as the large capacity obtained from electrochemical measurements confirms that lithiation of $NiPS_3$ in this voltage range is a multielectron process involving redox activities of both cations and anion. At 0.8 V, there is an absence of Bragg diffraction corresponding to the parent $NiPS_3$ $C2/m$ phase with all peaks corresponding to Li_2S (Figure S6). This electrochemical conversion process appears to be partially reversible during delithiation, as evidenced by the recovery of $NiPS_3$ peaks in the XRD spectra. However, the small peaks corresponding to the Li_2S phase remained at the end of the first cycle, confirming the partial irreversibility. The amorphization process upon Li insertion beyond the intercalation limit makes it problematic to gain a crystallographic understanding of the structural evolution of $NiPS_3$. However, the presence of Li_2S and amorphous thiophosphate-based compounds suggests that the likely pathway for decomposition reactions revolves around the formation and transformation of Li thiophosphate glass ceramics. Detailed investigations into the structural evolution of the possible thiophosphate units and the local bonding environment could illuminate the conversion reaction mechanisms related to the multielectron redox process. To this effort, *ex situ* Raman spectroscopy was performed at various states of charge to probe crystal structures and intermediate species from molecular vibrations.

In pristine $NiPS_3$, the thiophosphate anion $P_2S_6^{4-}$ forms ethane-like polyhedra with a P−P bond. The Raman spectrum (Figure 4c) of as-prepared $NiPS_3$ is consistent with previously reported literature[51] and shows strong E_g doubly degenerate modes with 514 nm excitation. The high-frequency peak at 133

https://doi.org/10.1021/acsami.1c19963
ACS Appl. Mater. Interfaces 2022, 14, 3980−3990

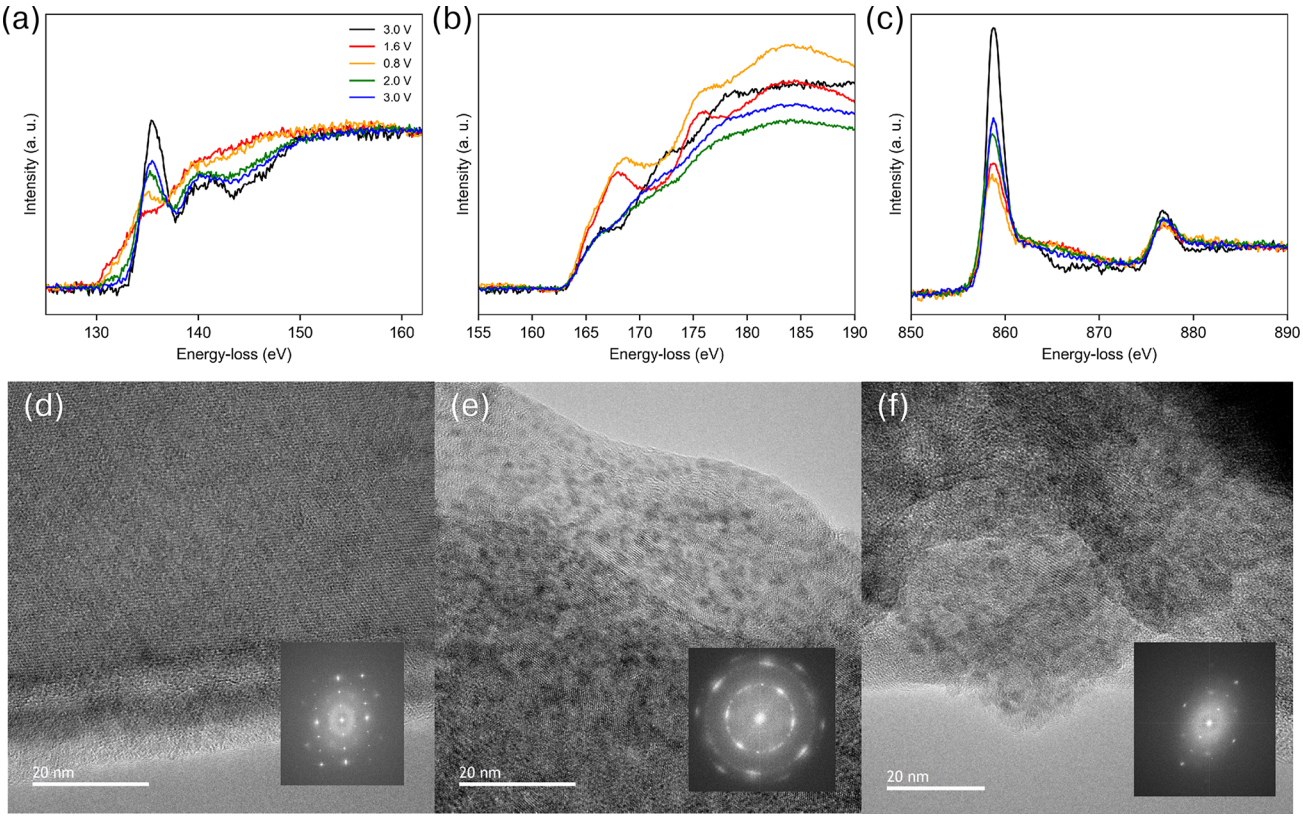

Figure 5. *Ex situ* EELS of (a) P L-edge, (b) S L-edge, and (c) Ni L-edge spectra. The EELS spectra provide insight concerning the electrochemical reversibility of the conversion process. HRTEM images and corresponding Fourier Transformations of (d) pristine $NiPS_3$ (e) after Li-ion insertion at 0.8 V and (f) after 1 cycle at 3 V.

cm^{-1} has been attributed to translational motions of Ni^{2+} cation,[52] but all other peaks in the frequency range correspond to PS_3^{2-} anions. Upon lithiation, all Raman bands assigned to motion of Ni^{2+} and PS_3^{2-} from $NiPS_3$ disappear, and a number of peaks around 300 and between 380 and 500 cm^{-1} emerge. Discharging to 1.6 V, notable peaks centered at 375, 410, and 435 cm^{-1} appear. These peaks are signatures of the E2, A1, and E3 symmetry species of the P−S bond and confirm the formation of other thiophoshate compounds consisting of PS_4^{3-} and $P_2S_7^{4-}$ polyhedra as a result of lithium insertion.[53−55] In particular, a lack of T_2 P═S groups (685 cm^{-2}) and a sharp A P═S mode (715 cm^{-2}) at 1.6 V suggests that the phosphorus sulfur compounds are still sulfur-rich in nature with the sulfur to phosphorus ratio below 1. Further lithiation below 1.6 V induces the active formation of Li_2S with sulfur reduction (evidenced by both XRD and Raman results), and correspondingly, phosphorus-rich polysulfidophosphate groups are formed. The destabilization of the anion structure and the cleavage of bonds upon substantial Li-ion insertion have also been predicted by our Monte Carlo simulation. With the continuous insertion of up to $x = 2$ and 3 in Li_xNiPS_3, the $P_2S_6^{4-}$ *hypo*-thiophosphate anion structure is significantly distorted, and the P−S bond is subsequently broken (Figure S7).

Considering reported Raman spectra in the literature of chemically lithiated Li_xNiPS_3, the chemically and electrochemically lithiated $NiPS_3$ produced drastically different spectra (Figure 4c).[52] The primary reason for this is that the driving force of chemical lithiation is considerably lower than that of electrochemical lithiation so that it does not induce formation of new phases.[56] The maximum amount of Li-ions intercalated via chemical lithiation was Li_xNiPS_3, $x = 1.16$ mol equiv. These chemically intercalated Li-ions occupy the vacant sites within the 2D layer. It was reported that the Raman normal mode positions were not shifted upon chemical lithiation, although a considerable decrease in intensity was observed.[52] This finding further confirms that the electrochemical lithiation process leading to complete disappearance of the normal mode peaks must involve the decomposition of the starting material and the formation of new phases, such as phosphorus sulfides.

One interesting phenomenon that has been captured by the Raman spectroscopy is that upon delithiation the bands attributed to decomposition products still dominate the Raman spectra, and the normal modes for pristine $NiPS_3$ do not recover, suggesting that this process is not completely reversible. Polysulfidophosphate groups with P_4S_{10+n} compositions are in general decent Li-ion battery active materials with redox potentials above 2.0 V.[54,57] Because our system lacks significant electrochemical redox activity above 2.0 V, the phosphorus- and sulfur-based decomposition products are likely partially reduced inorganic phosphides (i.e., Ni_xPS_y, Li_xPS_y). It is important to note that partially reduced phosphide intermediates could be good ionic conductors, but many of these compounds are electrochemically inactive and are used most often as a solid electrolyte in Li-ion batteries.[58,59] This mechanism correlates well with the irreversibility in the Raman spectra and electrochemical capacity fade observed in our system.

X-ray photoelectron spectroscopy (XPS) has been performed on cycled electrodes to further identify and elucidate redox activities during the first cycle (Figure 4d−g). The

https://doi.org/10.1021/acsami.1c19963
ACS Appl. Mater. Interfaces 2022, 14, 3980−3990

evolution of the XPS spectra core peaks was recorded at various degrees of lithiation (1.6 and 0.8 V) and delithiation (2.0 and 3.0 V). Upon lithium insertion, both Ni $2p_{3/2}$ and $2p_{1/2}$ peaks shift toward lower binding energies, and the intensity of the $2p_{3/2}$ and $2p_{1/2}$ satellite peaks is decreased, suggesting a change in the Ni 3d electron configuration. This reveals that the Ni^{2+} in the $NiPS_3$ starting material undergoes a multistep reduction process. The Ni^{2+} shows signs of partial reduction at 1.6 V, and the partial reduction continues with deep discharge (0.8 V vs Li/Li^+). The formation of heterogeneously reduced, near-amorphous transition metal has also been observed in other conversion material systems at the end of their first discharge.[60,61] Upon delithiation of $NiPS_3$ at 2.0 V vs Li/Li^+, the Ni 2p spectrum is comparable to the pristine material with a Ni^{2+} oxidation state and remains constant throughout the remainder of the delithiation process to 3.0 V vs Li/Li^+. Because of the near-surface sensitivity of XPS, the complete dynamics of conversion reactions cannot be captured as the Ni oxidation proceeds into the bulk of the material.

Similarly, for the $(P_2S_6)^{4-}$ cluster, it has been observed that the P 2p core-level shifts toward higher binding energies, while the S 2p peak shifts toward lower binding energies with the insertion of Li-ions. In previous literature, this trend is attributed to a charge redistribution around these atoms, as occurs in conversion reactions, due to the Li insertion and subsequent Ni reduction.[62] Specifically, one reason for the shift in S 2p peak position is that during the formation of Li_2S a higher net charge is distributed on the sulfur anions. Also, for these elements, upon the delithiation at 2.0 and 3.0 V, the spectra trends similarly to the pristine material. Overall, the reversibility of Ni, P, and S oxidation and reduction has been observed through XPS of elements during the first cycle.

To further probe multielectron redox processes in the key elements, their composition and local coordination effects with other elements were analyzed by using *ex situ* EELS for the P, S, and Ni $L_{2,3}$-edges (Figure 5a–c). The trend in EELS $L_{2,3}$-edge observations is consistent with earlier XPS results in that the energy-loss near-edge structure (ELNES) evolution based on elemental composition, local bonding, and oxidation state changes upon charging/discharging is reasonably reversible for all three elements. The changes in the ELNES fine structure may come from (1) the electron count around elements that affects the white line intensity, mirroring the unfilled density-of-states above the Fermi energy and/or (2) the point group symmetry, for which any distortion or lowering of the point symmetry will result in a lifting of the degeneracies in the unoccupied molecular orbitals and in peak broadening with additional orbital options for the electrons to excite into.[63]

One interesting observation here is that the change in the ELNES fine structure for P, S, and Ni is significant when the discharge voltage reaches 1.6 V, indicating these redox centers likely experience considerable valence changes and/or local structural distortion with the insertion of only 1.5 Li-ions. In particular, the P $L_{2,3}$-edge fine structure for the pristine material starts with P in a symmetric environment with tetrahedral point symmetry based on the thiophosphate anion structure. With Li-ion insertion, lowering of the intensity of the peak at 138 eV and increase in the pre-edge tail were evident in the 1.6 and 0.8 V spectra. This behavior can be attributed to both the redox reactions around phosphorus and distortion in the local point symmetry as predicted by earlier simulation result (Figure S7).[64,65] The re-emergence of the peak around 168 eV in the 2.0 and 3.0 V spectra during charge is consistent with a return to the more symmetric tetrahedral point symmetry and the initial valence state, suggesting that the process is partly reversible.

To support these spectroscopic observations, the theoretical EELS spectra with varying amounts of Li-ions were calculated based on the atomic positions of $Li_xNi_8P_8S_{24}$ structures as predicted by the plane-wave-based DFT coupled with a Monte Carlo method.[66] The EELS P L-edge fine structure simulations, as shown in Figure S8, indicate the same trend in peak shift, displaying reduction in the intensity of the low-energy peak and increase in the pre-edge tail with higher degree of lithiation. Overall, the calculation result matches with the experimental peak features, confirming that the evolution in experimental P L-edge EELS data was primarily due to the distorted structures and loss of local symmetry. In the case of the S $L_{2,3}$-edge, the emergence of more dominant fine structure in the 1.6 and 0.8 V discharge spectra is attributed to the formation of Li_2S that exhibits higher point symmetry around the S compared to the pristine $NiPS_3$.[67] This result agrees well with what we observed in XRD and in electron diffraction that the partial conversion of Li_2S has been observed upon the initial lithiation below 1.6 V.

With the Ni $L_{2,3}$-edge, the dominant effect altering the fine structure is the presence of a core excitation, which continues to be reduced with Li-ion insertion based on the correlation between the higher L_3 and L_2 ratio.[68,69] As with the S and P EELS spectra, the local environmental changes around Ni also appear to be partly reversible with the lithiation–delithiation process.

Overall, during the electrochemical cycling in the conversion region, a decent degree of reversibility has been evidenced based on structural evolution, key element valence state transitions, and changes in molecular symmetry from XRD, XPS, and EELS techniques. The Li-ion reaction mechanism of $NiPS_3$ during the first insertion–deinsertion process between 0.8 and 3.0 V (vs Li/Li^+) can be described as follows:

$$x\mathrm{Li}^+ + x\mathrm{e}^- + \mathrm{NiPS_3} \rightarrow \mathrm{Li}_x\mathrm{NiPS_3} \quad (x \leq 2) \tag{1}$$

$$x\mathrm{Li}^+ + x\mathrm{e}^- + \mathrm{Li_2NiPS_3} \rightarrow \mathrm{Li_2Ni}_{1-\delta}(\mathrm{PS_3})_{1-y} + \mathrm{Li_2}(\mathrm{PS}_{1+n})_y + \frac{x-2}{2}\mathrm{Li_2S} + \delta\mathrm{Ni}^0 \quad \left(2 < x < 6;\ 0 \leq y \leq 1;\ n = 3 - \frac{x-2}{2}\right) \tag{2}$$

$$x\mathrm{Li}^+ + x\mathrm{e}^- + \mathrm{Li_2NiPS_3} \rightarrow \mathrm{Li_3PS}_{4+n} + \frac{x-1}{2}\mathrm{Li_2S} + \mathrm{Ni}^0 \quad (2 < x < 4) \tag{3}$$

The Fourier transform of HRTEM images (Figure 5d–f and Figure S9) intriguingly provide further evidence for the formation of the crystalline parent $NiPS_3$ phase after cycling. However, the irreversible nature of conversion reactions was also observed from the Raman vibrational modes and poor electrochemical cyclability. The discrepancy can be reconciled by the nanoscale chemical inhomogeneity produced from electrochemically driven conversion reactions. The HRTEM images highlight significant morphological changes after cycling with regions of crystalline $NiPS_3$ and other amorphous phases. Because of incremental chemical inhomogeneity that develops every cycle, the pristine material is amorphized and

https://doi.org/10.1021/acsami.1c19963
ACS Appl. Mater. Interfaces 2022, 14, 3980–3990

decomposed to form electrochemically inactive species upon continuous charge/discharge process (Figures S10 and S11). Figure 6 summarizes the structure and phase evolution of $NiPS_3$ undergoing a series of complex redox reactions upon insertion/deinsertion of Li-ions.

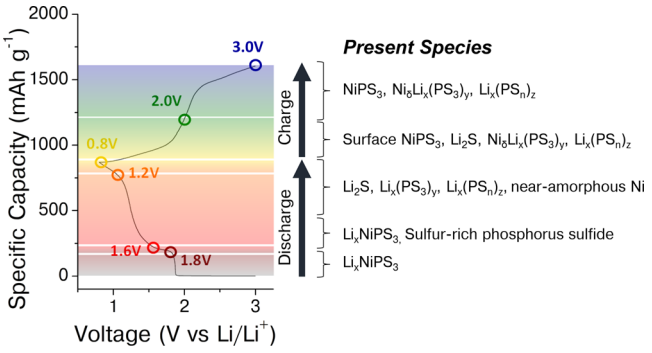

Figure 6. Galvanostatic profile with chemical species representing the redox processes occurring during the first discharge/charge cycle of $NiPS_3$.

CONCLUSION

In this study, we illuminate the lithiation process in $NiPS_3$ polyanionic materials, which undergo two-step intercalation and conversion reactions, sequentially. PDF and DFT Monte Carlo molecular dynamic simulations revealed that the lithium intercalation without phase transition occurs up to about 0.8 mol of Li per $NiPS_3$ unit, occupying the thermodynamically favorable Wyckoff sites. With continuous Li-ion insertion, the P−S anion structural backbone is destabilized, and the crystalline $NiPS_3$ host phase subsequently undergoes conversion reactions to form binary and ternary chemical moieties based on Li, Ni, P, and S. Our findings have revealed chemical and structural reversibility in the macroscopic representation of the electrochemical intercalation and conversion process occurs in $NiPS_3$ but have also successfully captured nanoscale inhomogeneity and formation of electrochemically inactive species that lead to poor long-term behavior. These findings highlight an important aspect of mechanistic studies that a combination of multiple characterization techniques is essential in capturing the complex chemical dynamics during electrochemical reactions. Insights into the electrochemical reaction mechanism, which might be common among phosphorus sulfide materials, should be helpful in the design of novel phosphorus and sulfur anion-based electrode materials.

EXPERIMENTAL SECTION

Lab X-ray diffraction was performed by using a P'analytical Empyrean. Refinement was performed by using GSAS-II.[70] The Pawley refinement was performed over a Q range of 0.38−4.83 Å^{-1} with a Pawley negative weighting factor of 0.001. Parameters that were refined included (1) lattice parameters, (2) sample displacement, (3) March−Dollase preferred orientation ratio, (4) peak shape, (5) peak position, (6) peak intensity, (7) background Chebyshev coefficients of degree eight, and (8) histogram scale factor separate from Pawley intensity refinement. Refinements utilized the following CIF file: ICSD-602341. SEM was performed by using an FEI Nova 230 Nano system. Half-cell galvanostatic cycling and cyclic voltammetry from 0.8 to 3.0 V at a current density of 100 mA g^{-2} and sweep rate of 0.1 mV s^{-1}, respectively, were performed. Electrochemical impedance spectroscopy between 1 MHz and 100 mHz using a 10 mV amplitude and bias at 0 V versus open circuit was performed periodically. Carbon Black Super P (+99%, Alfa Aeser), styrene−butadiene rubber (SBR, MTI Corp.), and carboxymethylcellulose (CMC, DOW Chemical) were used without further processing. Electrode slurries were made with 80 wt % active material, 10 wt % Super P, and 10 wt % CMC/SBR (4:6) dispersed in deionized water and doctor bladed onto a stainless-steel foil. Mass loading of the electrodes was typically 1.5−2 mg/cm^2 with a film thickness of approximately 30−40 μm. Raman spectroscopy was performed by using a Renishaw inVia confocal Raman microscope. The analysis was performed with a 514 nm Ar laser and 1800/mm grating through a 20× objective lens. XPS using a Kratos Axis Ultra with a monochromatic aluminum X-ray source was performed on the pristine $NiPS_3$ after dispersing from a methanol solution. The cycled electrodes were prepared by imposing the potentiostatic hold at a specified voltage for 30 min and transferred by using an inert-atmosphere chamber. Charge calibration was performed based on the adventitious carbon peak. Microstructural analysis was performed by using the scanning-TEM (STEM) mode on a JEOL 2100 field emission TEM, equipped with a high-resolution pole piece, and direct detection electron energy loss spectroscopy (EELS). X-ray absorption near edge structure (XANES) spectra were calculated by using FDMNES software. The atomic coordinates of lithiated $NiPS_3$ compounds were obtained from the DFT calculations.

For the computational effort, the plane-wave-based density functional theory package VASP was used to investigate the intercalation limit of Li.[71] The ion−electron interactions are described by using the projector augmented wave pseudopotentials,[72] and the exchange correlation functionals are treated within the generalized gradient approximation by Perdew, Burke, and Ernzerhof with a cutoff energy of 364 eV.[73,74] An on-site replacement of the exchange correlation functionals is necessary for the accurate description of the ground state because of the strongly correlated d electrons of nickel. Here the formalism by Dudarev is implemented with a Coulomb interaction parameter U of 7.15 eV and the interaction exchange parameter J of 0.95 eV.[75] The valence electron configurations are $3d^84s^2$, $3s^23p^3$, $3s^23p^4$, and $2s^1$ for nickel, phosphorus, sulfur, and lithium, respectively. A Monkhorst−Pack k-point mesh of 6 × 4 × 2 is used for the integration in the Brillouin zone.[76] The relaxation convergence criteria are 10^{-6} and 10^{-4} eV for electronic steps and ionic steps, respectively. A correction term from the DFT-D2 method by Grimme is also included to account for the long-range van der Waals interactions.[77]

ASSOCIATED CONTENT

Supporting Information

The Supporting Information is available free of charge at https://pubs.acs.org/doi/10.1021/acsami.1c19963.

Experimental data and analyses, including Figures S1−S11 and Table S1 (PDF)

AUTHOR INFORMATION

Corresponding Authors

Vicky Doan-Nguyen − *Department of Materials Science and Engineering, The Ohio State University, Columbus, Ohio 43212, United States; Department of Mechanical and Aerospace Engineering, The Ohio State University, Columbus, Ohio 43212, United States;* orcid.org/0000-0003-4204-3271; Email: doan-nguyen.1@osu.edu

Christopher Choi − *Department of Materials Science and Engineering, University of California, Los Angeles, Los Angeles, California 90095, United States;* orcid.org/0000-0001-5097-8443; Email: christopherchoi@ucla.edu

Authors

David Ashby − *Department of Materials Science and Engineering, University of California, Los Angeles, Los*

https://doi.org/10.1021/acsami.1c19963
ACS Appl. Mater. Interfaces 2022, 14, 3980−3990

Angeles, California 90095, United States; Sandia National Laboratories, Livermore, California 94550, United States

You Rao − *Department of Materials Science and Engineering, The Ohio State University, Columbus, Ohio 43212, United States*

Elaf Anber − *Department of Materials Science & Engineering, Johns Hopkins University, Baltimore, Maryland 21218, United States; Department of Materials Science and Engineering, Drexel University, Philadelphia, Pennsylvania 19104, United States*

James L. Hart − *Department of Materials Science & Engineering, Johns Hopkins University, Baltimore, Maryland 21218, United States;* orcid.org/0000-0002-2960-6925

Danielle Butts − *Department of Materials Science and Engineering, University of California, Los Angeles, Los Angeles, California 90095, United States;* orcid.org/0000-0002-8529-1227

Catrina Wilson − *Department of Materials Science and Engineering, The Ohio State University, Columbus, Ohio 43212, United States*

Emily Levin − *Materials Department, University of California, Santa Barbara, Santa Barbara, California 93106, United States;* orcid.org/0000-0002-8663-8018

Mitra Taheri − *Department of Materials Science & Engineering, Johns Hopkins University, Baltimore, Maryland 21218, United States*

Maryam Ghazisaeidi − *Department of Materials Science and Engineering, The Ohio State University, Columbus, Ohio 43212, United States*

Bruce Dunn − *Department of Materials Science and Engineering, University of California, Los Angeles, Los Angeles, California 90095, United States;* orcid.org/0000-0001-5669-4740

Complete contact information is available at: https://pubs.acs.org/10.1021/acsami.1c19963

Author Contributions

C.C. conducted electrochemical measurements, X-ray diffraction, and Raman spectroscopy, and analyzed all *ex situ* data. D.A. performed XPS measurements and analysis. E.L. and V.D.N. synthesized $NiPS_3$ powders. D.B. performed X-ray diffraction. C.E.W. performed Rietveld refinement, assisted in synchrotron data collection, and processed PDF data. E.A. and J.H. collected EELS and electron diffraction data. M.T. supervised TEM experiments. Y.R. and M.G. performed the DFT calculations and analysis. B.S.D. supervised the electrochemical measurements. C.C. and V.D.N. wrote the manuscript. D.A. and D.B. edited the manuscript. V.D.N. conceived of the original idea, supervised the findings of this work, and collected synchrotron X-ray scattering data. The manuscript was written through contributions of all authors. All authors have given approval to the final version of the manuscript.

Funding

V.D.N. gratefully acknowledges the start-up financial support from The Ohio State University, Oak Ridge Associated Universities Ralph E. Powe Junior Faculty Enhancement Award, and seed funding from The Ohio State University Materials Research Program. C.E.W. appreciatively acknowledges the National Science Foundation Graduate Research Fellowship Program. The research was supported in part by the Office of Naval Research (N00014-19-1-2113). M.G., Y.R., and V.D.N. acknowledge partial support by the Center for Emergent Materials, an NSF MRSEC, under Award DMR-2011876. M.L.T. and J.L.H. acknowledge funding in part from the US Department of Energy, Office of Basic Energy Sciences through contract DE-SC0020314. M.L.T. and E.A. were funded, in part, from the Office of Naval Research Multidisciplinary University Research Initiative (MURI) program through contract N00014-20-1-2368.

Notes

The authors declare no competing financial interest.

■ ACKNOWLEDGMENTS

This research used resources of the Advanced Photon Source (APS), a U.S. Department of Energy (DOE) Office of Science User Facility operated for the DOE Office of Science by Argonne National Laboratory under Contract DE-AC02-06CH11357. Research at the APS was conducted by using the general user proposal GUP-62602. V.D.N. acknowledges fruitful discussions and assistance from undergraduate researcher Patrice Crosby and Professor David McComb.

■ REFERENCES

(1) Murphy, D. W.; Di Salvo, F. J.; Carides, J. N. Vanadium Disulfide: Metal Substitution and Lithium Intercalation. *J. Solid State Chem.* **1979**, *29* (3), 339−343.

(2) Britto, S.; Leskes, M.; Hua, X.; Hebert, C.-A.; Shin, H. S.; Clarke, S.; Borkiewicz, O.; Chapman, K. W.; Seshadri, R.; Cho, J.; Grey, C. P. Multiple Redox Modes in the Reversible Lithiation of High-Capacity, Peierls-Distorted Vanadium Sulfide. *J. Am. Chem. Soc.* **2015**, *137* (26), 8499−8508.

(3) Butala, M. M.; Mayo, M.; Doan-Nguyen, V. V. T.; Lumley, M. A.; Göbel, C.; Wiaderek, K. M.; Borkiewicz, O. J.; Chapman, K. W.; Chupas, P. J.; Balasubramanian, M.; Laurita, G.; Britto, S.; Morris, A. J.; Grey, C. P.; Seshadri, R. Local Structure Evolution and Modes of Charge Storage in Secondary Li-FeS2 Cells. *Chem. Mater.* **2017**, *29* (7), 3070−3082.

(4) Du, Y.; Weng, W.; Zhang, Z.; He, Y.; Xu, J.; Sun, J.; Liao, J.; Bao, J.; Zhou, X. Candied-Haws-like Architecture Consisting of FeS_2 @C Core-Shell Particles for Efficient Potassium Storage. *ACS Materials Lett.* **2021**, *3* (4), 356−363.

(5) Butala, M. M.; Doan-Nguyen, V. V. T.; Lehner, A. J.; Gobel, C.; Lumley, M. A.; Arnon, S.; Wiaderek, K. M.; Borkiewicz, O. J.; Chapman, K. W.; Chupas, P. J.; Balasubramanian, M.; Seshadri, R. Operando Studies Reveal Structural Evolution with Electrochemical Cycling in Li-CoS2. *J. Phys. Chem. C* **2018**, *122* (43), 24559−24569.

(6) Xu, Y.; Sun, J.; He, Y.; Li, J.; Xu, J.; Sun, Y.; Liao, J.; Zhou, X. Construction of CoS2 Nanoparticles Embedded in Well-Structured Carbon Nanocubes for High-Performance Potassium-Ion Half/Full Batteries. *Sci. China Chem.* **2021**, *64* (8), 1401−1409.

(7) Sen, U. K.; Johari, P.; Basu, S.; Nayak, C.; Mitra, S. An Experimental and Computational Study to Understand the Lithium Storage Mechanism in Molybdenum Disulfide. *Nanoscale* **2014**, *6* (17), 10243−10254.

(8) Doan-Nguyen, V. V. T.; Subrahmanyam, K. S.; Butala, M. M.; Gerbec, J. A.; Islam, S. M.; Kanipe, K. N.; Wilson, C. E.; Balasubramanian, M.; Wiaderek, K. M.; Borkiewicz, O. J.; Chapman, K. W.; Chupas, P. J.; Moskovits, M.; Dunn, B. S.; Kanatzidis, M. G.; Seshadri, R. Molybdenum Polysulfide Chalcogels as High-Capacity, Anion-Redox-Driven Electrode Materials for Li-Ion Batteries. *Chem. Mater.* **2016**, *28*, 8357−8365.

(9) Anasori, B.; Lukatskaya, M. R.; Gogotsi, Y. 2D Metal Carbides and Nitrides (MXenes) for Energy Storage. *Nature Reviews Materials* **2017**, *2*, 16098.

(10) Hong Ng, V. M.; Huang, H.; Zhou, K.; Lee, P. S.; Que, W.; Xu, J. Z.; Kong, L. B. Recent Progress in Layered Transition Metal Carbides and/or Nitrides (MXenes) and Their Composites: Synthesis and Applications. *J. Mater. Chem. A* **2017**, *5* (7), 3039−3068.

(11) Du, Y.; Weng, W.; Zhang, Z.; He, Y.; Xu, J.; Yang, T.; Bao, J.; Zhou, X. Double-Coated Fe2N@TiO_2@C Yolk-Shell Submicrocubes as an Advanced Anode for Potassium-Ion Batteries. *Chin. J. Chem.* **2021**, *39* (7), 1878−1884.
(12) Rousse, G.; Tarascon, J. M. Sulfate-Based Polyanionic Compounds for Li-Ion Batteries: Synthesis, Crystal Chemistry, and Electrochemistry Aspects. *Chem. Mater.* **2014**, *26* (1), 394−406.
(13) Manthiram, A.; Goodenough, J. B. Lithium Insertion into Fe2(SO4)3 Frameworks. *J. Power Sources* **1989**, *26* (3−4), 403−408.
(14) Nanjundaswamy, K. Synthesis, Redox Potential Evaluation and Electrochemical Characteristics of NASICON-Related-3D Framework Compounds. *Solid State Ionics* **1996**, *92* (1−2), 1−10.
(15) *Intercalation Chemistry*; Elsevier: 1982.
(16) Brec, R. Review on Structural and Chemical Properties of Transition Metal Phosphorous Trisulfides MPS 3. *Solid State Ionics* **1986**, *22*, 3−30.
(17) Zaanen, J.; Sawatzky, G. A.; Allen, J. W. Band Gaps and Electronic Structure of Transition-Metal Compounds. *Phys. Rev. Lett.* **1985**, *55* (4), 418−421.
(18) Brec, R.; Ouvrard, G.; Louisy, A.; Rouxel, J.; Le Mehaute, A. The Influence, on Lithium Electrochemical Intercalation, of Bond Ionicity in Layered Chalcogenophosphates of Transition Metals. *Solid State Ionics* **1982**, *6*, 185−190.
(19) Liang, Q.; Zheng, Y.; Du, C.; Luo, Y.; Zhang, J.; Li, B.; Zong, Y.; Yan, Q. General and Scalable Solid-State Synthesis of 2D MPS_3 (M = Fe, Co, Ni) Nanosheets and Tuning Their Li/Na Storage Properties. *Small Methods* **2017**, *1* (1−10), 1700304.
(20) Foot, P. J. S.; Katz, T.; Patel, S. N.; Nevett, B. A.; Pieecy, A. R.; Balchin, A. A. The Structures and Conduction Mechanisms of Lithium-Intercalated and Lithium-Substituted Nickel Phosphorus Trisulphide (NiPS$_3$), and the Use of the Material as a Secondary Battery Electrode. *Physica Status Solidi (a)* **1987**, *100*, 11−29.
(21) Brec, R.; Prouzet, E.; Ouvrard, G. Transition Metal Displacement in Cathodic Host Structures upon Lithium Intercalation. *J. Power Sources* **1993**, *43* (1−3), 277−288.
(22) Kuzminskii, Y. V.; Voronin, B. M.; Redin, N. N. Iron and Nickel Phosphorus Trisulfides as Electroactive Materials for Primary Lithium Batteries. *J. Power Sources* **1995**, *55* (2), 133−141.
(23) Kuz'minskii, Y. V.; Voronin, B. M.; Petrushina, I. M.; Redin, N. N.; Prikhodko, G. P. Nickel Phosphorus Trisulfide: An Electroactive Material for Medium-Temperature Lithium Batteries. *J. Power Sources* **1995**, *55* (1), 1−6.
(24) Wang, Z.; Li, X.; Yang, Y.; Cui, Y.; Pan, H.; Wang, Z.; Chen, B.; Qian, G. Highly Dispersed β-NiS Nanoparticles in Porous Carbon Matrices by a Template Metal-Organic Framework Method for Lithium-Ion Cathode. *J. Mater. Chem. A* **2014**, *2* (21), 7912.
(25) Liu, X. J.; Xu, Z. Z.; Ahn, H. J.; Lyu, S. K.; Ahn, I. S. Electrochemical Characteristics of Cathode Materials NiS2 and Fe-Doped NiS2 Synthesized by Mechanical Alloying for Lithium-Ion Batteries. *Powder Technol.* **2012**, *229*, 24−29.
(26) Gillot, F.; Boyanov, S.; Dupont, L.; Doublet, M.-L.; Morcrette, M.; Monconduit, L.; Tarascon, J.-M. Electrochemical Reactivity and Design of NiP $_2$ Negative Electrodes for Secondary Li-Ion Batteries. *Chem. Mater.* **2005**, *17* (25), 6327−6337.
(27) Piacentini, M.; Khumalo, F. S.; Olson, C. G.; Anderegg, J. W.; Lynch, D. W. Optical Transitions, XPS, Electronic States in NiPS3. *Chem. Phys.* **1982**, *65* (3), 289−304.
(28) Curro, G. M.; Grasso, V.; Neri, F.; Silipigni, L. The Effects of the Lithium Intercalation on the X-Ray Photoelectron Spectra of $NiPS_3$. *Il Nuovo Cimento* **1995**, *17* (1), 37−52.
(29) Piacentini, M.; Khumalo, F. S.; Leveque, G.; Olson, C. G.; Lynch, D. W. X-Ray Photoemission and Optical Spectra of $NiPS_3$, $FePS_3$ and $ZnPS_3$. *Chem. Phys.* **1982**, *72*, 61−71.
(30) Kuo, C.-T.; Balamurugan, K.; Shiu, H. W.; Park, H. J.; Sinn, S.; Neumann, M.; Han, M.; Chang, Y. J.; Chen, C.-H.; Kim, H.-D.; Park, J.-G.; Noh, T. W. The Energy Band Alignment at the Interface between Mechanically Exfoliated Few-Layer NiPS3 Nanosheets and ZnO. *Curr. Appl. Phys.* **2016**, *16* (3), 404−408.
(31) Novák, P.; Joho, F.; Imhof, R.; Panitz, J.-C.; Haas, O. In Situ Investigation of the Interaction between Graphite and Electrolyte Solutions. *J. Power Sources* **1999**, *81*−*82*, 212−216.
(32) Cabana, J.; Monconduit, L.; Larcher, D.; Palacín, M. R. Beyond Intercalation-Based Li-Ion Batteries: The State of the Art and Challenges of Electrode Materials Reacting through Conversion Reactions. *Adv. Mater.* **2010**, *22* (35), 170−192.
(33) Grugeon, S.; Laruelle, S.; Dupont, L.; Tarascon, J.-M. An Update on the Reactivity of Nanoparticles Co-Based Compounds towards Li. *Solid State Sci.* **2003**, *5* (6), 895−904.
(34) Foot, P.; Nevett, B. Lithium Ion Diffusion in Li_xNiPS_3 Single Crystals. *Solid state ionics* **1983**, *8*, 169−172.
(35) Whittingham, M. S. Lithium Batteries and Cathode Materials. *Chem. Rev.* **2004**, *104* (10), 4271−4302.
(36) Reimers, J. N.; Dahn, J. R. Electrochemical and In Situ X-Ray Diffraction Studies of Lithium Intercalation in Li x CoO2. *J. Electrochem. Soc.* **1992**, *139* (8), 2091−2097.
(37) Butala, M. M.; Mayo, M.; Doan-Nguyen, V. V. T.; Lumley, M. A.; Gobel, C.; Wiaderek, K. M.; Borkiewicz, O. J.; Chapman, K. W.; Chupas, P. J.; Balasubramanian, M.; Laurita, G.; Britto, S.; Morris, A. J.; Grey, C. P.; Seshadri, R. Local Structure Evolution and Modes of Charge Storage in Secondary Li-FeS2 Cells. *CHEMISTRY OF MATERIALS* **2017**, *29* (7), 3070−3082.
(38) Hua, X.; Robert, R.; Du, L.-S.; Wiaderek, K. M.; Leskes, M.; Chapman, K. W.; Chupas, P. J.; Grey, C. P. Comprehensive Study of the CuF_2 Conversion Reaction Mechanism in a Lithium Ion Battery. *J. Phys. Chem. C* **2014**, *118* (28), 15169−15184.
(39) Berthier, C.; Chabre, Y.; Segransan, P. NMR Studies of Lamellar Intercalation Compounds. *Physica B* **1980**, *99*, 107−116.
(40) Brec, R.; Schleich, D. M.; Ouvrard, G.; Louisy, A.; Rouxel, J. Physical Properties of Lithium Intercalation Compounds of the Layered Transition-Metal Chalcogenophosphites. *Inorg. Chem.* **1979**, *18* (7), 1814−1818.
(41) Ichimura, K.; Sano, M. Electrical Conductivity of Layered Transition-Metal Phosphorus Trisulfide Crystals. *Synth. Met.* **1991**, *45* (2), 203−211.
(42) Grasso, V.; Neri, F.; Santangelo, S.; Silipigni, L.; Piacentini, M. Electronic Transport Properties of NiPS3. *Phys. Rev. B* **1988**, *37* (9), 4419−4424.
(43) Borkiewicz, O. J.; Shyam, B.; Wiaderek, K. M.; Kurtz, C.; Chupas, P. J.; Chapman, K. W. The AMPIX Electrochemical Cell: A Versatile Apparatus for In Situ X-Ray Scattering and Spectroscopic Measurements. *J. Appl. Crystallogr.* **2012**, *45* (1), 1261−1269.
(44) Suto, Y.; Fujii, Y.; Miura AkiraRosero-Navarro, N. C.; Higuchi, M.; Tadanaga, K. Synthesis of Submicron-Sized NiPS3 Particles and Electrochemical Properties as Active Materials in All-Solid-State Lithium Batteries. *J. Ceram. Soc. Jpn.* **2018**, *126*, 568−572.
(45) Berthier, C.; Chabre, Y.; Minier, M. NMR Investigation of the Layered Transition Metal Phosphorus Trichalcogenides and the Intercalation Compounds LixNiPS3. *Solid State Commun.* **1978**, *28* (4), 327−332.
(46) Chianelli, R. R.; Dines, M. B. Reaction of N-Butyllithium with Transition Metal Trichalcogenides. *Inorg. Chem.* **1975**, *14* (10), 2417−2421.
(47) Trosset, J.-Y.; Scheraga, H. A. Reaching the Global Minimum in Docking Simulations: A Monte Carlo Energy Minimization Approach Using Bezier Splines. *Proc. Natl. Acad. Sci. U. S. A.* **1998**, *95* (14), 8011−8015.
(48) Wang, Y.; Ma, Y. Perspective: Crystal Structure Prediction at High Pressures. *J. Chem. Phys.* **2014**, *140* (4), 040901.
(49) Lin, C.-Y.; Power, P. P. Complexes of Ni(I): A "Rare" Oxidation State of Growing Importance. *Chem. Soc. Rev.* **2017**, *46* (17), 5347−5399.
(50) Hannah, D. C.; Sai Gautam, G.; Canepa, P.; Ceder, G. On the Balance of Intercalation and Conversion Reactions in Battery Cathodes. *Adv. Energy Mater.* **2018**, *8* (20), 1800379.
(51) Kuo, C. T.; Neumann, M.; Balamurugan, K.; Park, H. J.; Kang, S.; Shiu, H. W.; Kang, J. H.; Hong, B. H.; Han, M.; Noh, T. W.; Park,

https://doi.org/10.1021/acsami.1c19963
ACS Appl. Mater. Interfaces 2022, 14, 3980−3990

J. G. Exfoliation and Raman Spectroscopic Fingerprint of Few-Layer $NiPS_3$ Van Der Waals Crystals. *Sci. Rep.* **2016**, *6*, 1−10.
(52) Kerrache, I.; Julienat, C.; Sourisseaub, C. Raman Scattering Studies of Lithium-Intercalated $NiPS_3$. *Solid State Ionics* **1996**, *92*, 37−43.
(53) Ohara, K.; Mitsui, A.; Mori, M.; Onodera, Y.; Shiotani, S.; Koyama, Y.; Orikasa, Y.; Murakami, M.; Shimoda, K.; Mori, K.; Fukunaga, T.; Arai, H.; Uchimoto, Y.; Ogumi, Z. Structural and Electronic Features of Binary Li2S-P2S5 Glasses. *Sci. Rep* **2016**, *6* (1), 21302.
(54) Lin, Z.; Liu, Z.; Fu, W.; Dudney, N. J.; Liang, C. Lithium Polysulfidophosphates: A Family of Lithium-Conducting Sulfur-Rich Compounds for Lithium-Sulfur Batteries. *Angewandte Chemie - International Edition* **2013**, *52* (29), 7460−7463.
(55) Preefer, M. B.; Oschmann, B.; Hawker, C. J.; Seshadri, R.; Wudl, F. High Sulfur Content Material with Stable Cycling in Li-S Batteries. *Angew. Chem., Int. Ed.* **2017**, *56*, 15118.
(56) Hibble, S. The Chemical and Electrochemical Lithiation of CuO: An Analytical, Electron Microscopy Investigation. *Solid State Ionics* **1990**, *39* (3−4), 289−295.
(57) Li, X.; Liang, J.; Lu, Y.; Hou, Z.; Cheng, Q.; Zhu, Y.; Qian, Y. Sulfur-Rich Phosphorus Sulfide Molecules for Use in Rechargeable Lithium Batteries. *Angew. Chem., Int. Ed.* **2017**, *56* (11), 2937−2941.
(58) Nazri, G. Preparation, Structure and Ionic Conductivity of Lithium Phosphide. *Solid State Ionics* **1989**, *34* (1−2), 97−102.
(59) Lau, J.; Deblock, R. H.; Butts, D. M.; Ashby, D. S.; Choi, C. S.; Dunn, B. S. Sulfide Solid Electrolytes for Lithium Battery Applications. *Adv. Energy Mater.* **2018**, *8*, 1800933.
(60) Butala, M. M.; Danks, K. R.; Lumley, M. A.; Zhou, S.; Melot, B. C.; Seshadri, R. MnO Conversion in Li-Ion Batteries: In Situ Studies and the Role of Mesostructuring. *ACS Appl. Mater. Interfaces* **2016**, *8* (10), 6496−6503.
(61) Bock, D. C.; Pelliccione, C. J.; Zhang, W.; Timoshenko, J.; Knehr, K. W.; West, A. C.; Wang, F.; Li, Y.; Frenkel, A. I.; Takeuchi, E. S.; Takeuchi, K. J.; Marschilok, A. C. Size Dependent Behavior of Fe_3O_4 Crystals during Electrochemical (de)Lithiation: An in Situ X-Ray Diffraction, Ex Situ X-Ray Absorption Spectroscopy, Transmission Electron Microscopy and Theoretical Investigation. *Phys. Chem. Chem. Phys.* **2017**, *19* (31), 20867−20880.
(62) Currò, G. M.; Grasso, V.; Neri, F.; Silipigni, L. The Effects of the Lithium Intercalation on the X-Ray Photoelectron Spectra of NiPS3. *Il Nuovo Cimento D* **1995**, *17* (1), 37−52.
(63) Williams, D. B.; Carter, C. B. *Transmission Electron Microscopy*; Springer US: Boston, MA, 2009.
(64) Favron, A.; Gaufrès, E.; Fossard, F.; Phaneuf-L'Heureux, A.-L.; Tang, N. Y.-W.; Lévesque, P. L.; Loiseau, A.; Leonelli, R.; Francoeur, S.; Martel, R. Photooxidation and Quantum Confinement Effects in Exfoliated Black Phosphorus. *Nat. Mater.* **2015**, *14* (8), 826−832.
(65) Liu, X.; Wood, J. D.; Chen, K.-S.; Cho, E.; Hersam, M. C. In Situ Thermal Decomposition of Exfoliated Two-Dimensional Black Phosphorus. *J. Phys. Chem. Lett.* **2015**, *6* (5), 773−778.
(66) Joly, Y. X-Ray Absorption near-Edge Structure Calculations beyond the Muffin-Tin Approximation. *Phys. Rev. B* **2001**, *63* (12), 125120.
(67) Cabelguen, P.-E. *Advanced Research on Lithium-Sulfur Battery: Studies of Lithium Polysulfides*; The University of Waterloo: 2013.
(68) Leapman, R. D.; Grunes, L. A.; Fejes, P. L. Study of the L 23 Edges in the 3 d Transition Metals and Their Oxides by Electron-Energy-Loss Spectroscopy with Comparisons to Theory. *Phys. Rev. B* **1982**, *26* (2), 614−635.
(69) Pearson, D. H.; Ahn, C. C.; Fultz, B. White Lines and *d* -Electron Occupancies for the 3 *d* and 4 *d* Transition Metals. *Phys. Rev. B* **1993**, *47* (14), 8471−8478.
(70) Toby, B. H. EXPGUI, a Graphical User Interface for GSAS. *J. Appl. Crystallogr.* **2001**, *34*, 210−213.
(71) Kresse, G.; Furthmüller, J. Efficient Iterative Schemes for *Ab Initio* Total-Energy Calculations Using a Plane-Wave Basis Set. *Phys. Rev. B* **1996**, *54* (16), 11169−11186.
(72) Kresse, G.; Joubert, D. From Ultrasoft Pseudopotentials to the Projector Augmented-Wave Method. *Phys. Rev. B* **1999**, *59* (3), 1758−1775.
(73) Langreth, D. C.; Mehl, M. J. Beyond the Local-Density Approximation in Calculations of Ground-State Electronic Properties. *Phys. Rev. B* **1983**, *28* (4), 1809−1834.
(74) Perdew, J. P.; Burke, K.; Ernzerhof, M. Generalized Gradient Approximation Made Simple. *Phys. Rev. Lett.* **1996**, *77* (18), 3865−3868.
(75) Dudarev, S. L.; Botton, G. A.; Savrasov, S. Y.; Humphreys, C. J.; Sutton, A. P. Electron-Energy-Loss Spectra and the Structural Stability of Nickel Oxide: An LSDA+U Study. *Phys. Rev. B* **1998**, *57* (3), 1505−1509.
(76) Monkhorst, H. J.; Pack, J. D. Special Points for Brillouin-Zone Integrations. *Phys. Rev. B* **1976**, *13* (12), 5188−5192.
(77) Grimme, S. Semiempirical GGA-Type Density Functional Constructed with a Long-Range Dispersion Correction. *J. Comput. Chem.* **2006**, *27* (15), 1787−1799.

https://doi.org/10.1021/acsami.1c19963
ACS Appl. Mater. Interfaces 2022, 14, 3980−3990